Mon. Not. R. Astron. Soc. **426,** 2107–2114 (2012) doi:10.1111/j.1365-2966.2012.21864.x

A 20 GHz bright sample for $\delta > +72°$ – I. Catalogue

S. Righini,[1⋆] E. Carretti,[2] R. Ricci,[1] A. Zanichelli,[1] K.-H. Mack,[1] M. Massardi,[1] I. Prandoni,[1] P. Procopio,[3,4] R. Verma,[1] M. López-Caniego,[5] L. Gregorini[1,6] and F. Mantovani[1]

[1]*INAF – IRA Bologna, Via Gobetti 101, I-40129 Bologna, Italy*
[2]*CSIRO Astronomy and Space Science, PO Box 276, Parkes, NSW 2870, Australia*
[3]*INAF – IASF Bologna, Via Gobetti 101, I-40129 Bologna, Italy*
[4]*School of Physics, David Caro Building, Corner of Tin Alley & Swanston Street, University of Melbourne, Parkville, VIC 3010, Australia*
[5]*Instituto de Física de Cantabria (CSIC-UC), Avda. los Castros s/n, 39005 Santander, Spain*
[6]*Dipartimento di Astronomia, Universitá di Bologna, via Ranzani 1, I-40127 Bologna, Italy*

Accepted 2012 August 5. Received 2012 August 3; in original form 2012 June 29

ABSTRACT

During 2010–11, the Medicina 32-m dish hosted the seven-feed 18–26.5 GHz receiver built for the Sardinia Radio Telescope, with the goal to perform its commissioning. This opportunity was exploited to carry out a pilot survey at 20 GHz over the area for $\delta > +72.^{\circ}3$. This paper describes all the phases of the observations, as they were performed using new hardware and software facilities. The map-making and source extraction procedures are illustrated. A customized data reduction tool was used during the follow-up phase, which produced a list of 73 confirmed sources down to a flux density of 115 mJy. The resulting catalogue, presented here, is complete above 200 mJy. Source counts are in agreement with those provided by the Australia Telescope 20 GHz (AT20G) survey. This pilot activity paves the way for a larger project, the *K*-band Northern Wide Survey (KNoWS), whose final aim is to survey the whole Northern hemisphere down to a flux limit of 50 mJy (5σ).

Key words: methods: observational – galaxies: active – radio continuum: general.

1 INTRODUCTION

Extragalactic radio sources extracted from high-frequency (>10 GHz) surveys are expected to have a major impact on astrophysics. They can provide samples of rare classes of sources with flat or inverted spectrum, which, at low frequencies, are swamped by more numerous populations that fade away as the frequency increases (for a review, see De Zotti et al. 2010).

They can hence open a window to new classes of sources, such as those with strong synchrotron or free–free self-absorption corresponding to both very early phases of nuclear radioactivity (extreme GHz-peaked-spectrum sources or high-frequency peakers) and late phases of the evolution of active galactic nuclei, characterized by low accretion/radiative efficiency (ADAF/ADIOS sources), as well as to early phases of the evolution of radio afterglows of gamma-ray bursts. In this context, the comparison with the ongoing *Fermi* observations will yield very interesting results (see Mahony et al. 2010).

These sources also play a vital role in the interpretation of temperature and polarization maps of the cosmic microwave background (CMB). Extragalactic point sources are one of the major foreground emissions (Toffolatti et al. 2005; Leach et al. 2008; Planck Collaboration 2011c); the knowledge of their positions and flux densities is crucial to remove their contribution and to estimate the residual error due to faint and unresolved components in CMB maps. As the source population composition changes at high frequency, cleaning procedures based on lower frequency catalogues are unreliable, making it essential to carry out surveys at frequencies close to the CMB window (centred at 60–70 GHz). In addition, as the *Planck* satellite is now active, the realization of a coeval 20-GHz blind survey helps, when selecting flux density limits, in avoiding errors induced by high-frequency variability.

High-frequency sky surveys have become feasible very recently. Because of the faint signal, the existing surveys at 10–100 GHz usually cover small areas with good sensitivity [e.g. Very Small Array (VSA) at 34 GHz with $S_{\rm lim} = 100$ mJy; Gawroński et al. 2010] or consist of all-sky shallow surveys [e.g. *WMAP* at 23, 33, 41, 64 and 94 GHz with $S_{\rm lim} > 1$ Jy (Wright et al. 2009a,b) and Early Release Compact Source Catalogue (ERCSC) at 30, 44, 70 and 100 GHz (Planck Collaboration 2011a,b,c)]. The only exception to this is the all-southern-sky Australia Telescope 20 GHz (AT20G) survey, which observed the entire southern sky with the Australia Telescope Compact Array, detecting around 6000 sources down to a flux density limit of 50 mJy (Murphy et al. 2010; Massardi et al. 2011).

⋆E-mail: s.righini@ira.inaf.it

This calls for a northern sky survey with equivalent sensitivity to complete the coverage of the entire sky. Such a completeness is particularly important for several aims for which a statistical information is not sufficient, such as the study of the SED of peculiar objects and the selection of samples at high radio frequency for the northern or whole sky. A precise position of all the sources is also required to flag out the contaminated pixels from CMB maps.

The availability of a *K*-band (namely 18–26.5 GHz) multifeed (MF) receiver installed on a medium-sized antenna such as the Medicina 32-m dish, having a beam size of 1.6 arcmin at 21 GHz, gave us the possibility to execute a pilot survey to verify the receiver performance, together with new software tools, while exploring a sky area which had never been extensively observed at these frequencies. This test activity paved the way for a larger project, the *K*-band Northern Wide Survey (KNoWS), which aims at performing a blind survey over the whole Northern hemisphere, with a sensitivity of 50 mJy (5σ).

The outline of the paper is the following. After a description of the system capabilities (Section 2), we summarize in Section 3 the survey strategy, including the map-making and source extraction techniques applied to achieve the list of candidate sources. The 20-GHz follow-up observations are described in Section 4, together with the automatic pipeline produced for the data reduction. Finally, the catalogue is presented in Section 5 and results are summarized in Section 6. A separate paper by Ricci et al. (in preparation, hereafter Paper II) illustrates the detailed spectral index analysis of the sources.

2 THE OBSERVING SYSTEM

The Medicina dish is a 32-m parabolic antenna located 35 km southeast of Bologna (Italy). It is operated by the Istituto di Radioastronomia (IRA), which is part of the Istituto Nazionale di Astrofisica (INAF). The 18–26.5 GHz MF receiver consists of seven corrugated horns in hexagonal layout, each providing left-handed circular polarization (LCP) and right-handed circular polarization (RCP) output channels, for a total of 14 channels. The instantaneous bandwidth of each channel is 2 GHz. Reference values for the system performances are provided in Table 1. We note that the decreasing gain for the lowest frequency range is due to poor illumination of the feeds: the receiver was developed for the Sardinia Radio Telescope, and consequently it was not optimized for the Medicina dish.

The broad total bandwidth delivered by the MF outputs (28 GHz) is detected by an analogue total power backend, expressly produced for its use with the MF receiver. The main specifications of this backend are summarized in Table 2. Both these hardware components were developed by the Institute of Radioastronomy (INAF) for the new Sardinia Radio Telescope, but were installed on the Medicina dish to undergo the commissioning phase.

Table 1. *K*-band MF main features, for elevation 45°, $\tau = 0.1$.

Frequency (GHz)	Beam size (arcmin)	T_{sys} (K)	Gain (K Jy^{-1})
18	1.7	43	0.10
22	1.4	72	0.11
26	1.2	79	0.11

3 SURVEY TEST OBSERVATIONS

In 2010 winter, we produced a total intensity test map covering the Northern polar cap (∼880 deg^2, $\delta > 72.^\circ3$), which allowed us to deeply check the new hardware and software facilities – the MF, the analogue continuum backend and the telescope control system – which is a new system based on the ALMA Common Software (see Orlati et al. 2012). The actually chosen band, due to RFI constraints, was 20–22 GHz.

The observing strategy consisted of long and fast (15° min^{-1}) on-the-fly (OTF) azimuth scans – i.e. at constant elevation. This technique was based on that developed for the project S-PASS at the Parkes radiotelescope (Carretti 2010; Carretti et al., in preparation). To optimize the area scanned by the seven beams, the MF array was rotated by an angle $\alpha = 19.^\circ1$ with respect to its rest position. This way, the paths run by the individual beams were equally spaced in elevation realizing a regular sampling of the sky. Fig. 1 shows the projected beams in the horizontal reference frame.

The apparent rotation of the celestial sphere was exploited to cover the sky area to map, which was a 'declination strip' spanning 24 h in right ascension (RA). In a single sidereal day, this technique allowed us to observe, in the equatorial frame, 'wavy' stripes within the belt (see fig. 8 in Carretti 2010). To complete the map, this scheme was repeated in the following days, shifting the stripe pattern to fill in the missing areas until the Nyquist sampling, at least, was reached. In practice, this translated into starting the azimuth scan sequence at a different LST. The sidereal-time interleave between two adjacent sequences was computed so that the stripes covered by the scans were spaced by half a beam size or less. In particular, the interleave produced the Nyquist sampling for the outer region of the map, while the inner area reached a higher sampling.

Table 2. Total power backend characteristics.

IF inputs	14 × 3, in the range 0.1–2.1 GHz
IF outputs	2, in the range 0.1–2.1 GHz
Instant bandwidth	Selectable: 150, 680, 1200 and 2000 MHz
Cable equalization	Up to 12 dB
Attenuators	Variable: 0–15 dB
Resolution	Up to 21 bit
Sampling interval	0.001–1 s
Noise source	Chopping frequency: 0.5–500 Hz

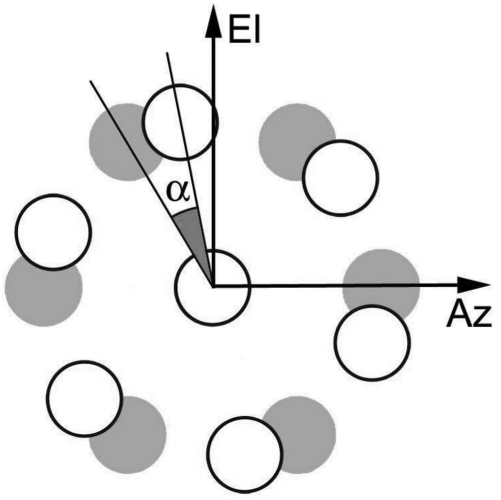

Figure 1. The projected beams in the Az–El frame. Empty circles correspond to the rotated position, filled circles to the rest position.

Observing at a constant elevation is extremely helpful for both data stability and calibration. Ground emission is mainly elevation dependent, and the same holds for atmospheric opacity: when observing in steady, uniform weather conditions such as in a dry, clear day, the opacity is only a function of the airmass.

The flux density calibration of the map was achieved byobserving calibrators (3C 286, 3C 295, 3C 48 and 3C 123) at least four times a day, when each of them transited at the same elevation of the horizontal scans. As weather conditions during the observations were quite stable, this simplification was acceptable to calibrate each of the 24-h-long data sets.

Fast scans allowed us to cover the chosen polar cap area with declination (Dec.) in the range [+ 72.°3, +89°] in 4 d. Specifically, scans were performed at 15° min^{-1} between 1° and 25° of azimuth, taken at elevation 44.°52.

3.1 Theoretical sensitivity

A single OTF scan has a theoretical instantaneous noise which can be computed by means of the radiometer equation (as in Rohlfs & Wilson 2006):

$$\sigma_S = \frac{kT_{sys}}{G\sqrt{Bt}}\ (\mathrm{Jy\,beam^{-1}}), \qquad (1)$$

where $k = 1$ for a single polarization, G is the antenna gain (K Jy^{-1}), B is the bandwidth (Hz) and t is the integration time (s). As a reference value to assess the expected performance of the system, we use the 1-s integration sensitivity, which reads $\sigma_{1s} = 14.6$ mJy beam^{-1} for a single polarization, for observations carried out at 21 GHz with a bandwidth of 2 GHz (values for T_{sys} and gain are extrapolated from Table 1).

We now achieve a first-order estimate of the theoretical noise level of a map obtained exploiting the above-mentioned scanning strategy. The following computation refers to the integration of OTF scans in the 20–22 GHz band, performed at the constant elevation El = 45°, considering the following:

(i) the actual scan speed on sky is 15° min^{-1} cos(El) = 10.°7 min^{-1};

(ii) one beam-sized pixel (1.6 arcmin) is observed for 0.150 s in each individual subscan;

(iii) the scanning strategy includes back and forth scans. Along with the proper spacing between adjacent subscans (half a beamwidth), this leads us to observe a beam-sized pixel for four times, for a total integration time $t = 0.600$ s;

(iv) every feed observes two circular polarizations, which further improves the sensitivity by a factor of $\sqrt{2}$, since $k = 1/\sqrt{2}$ for dual polarization.

Equation (1) thus yields $\sigma_S = 13.4$ mJy beam^{-1}, as concerns the less sampled area of the map – i.e. its southern edge (see Section 3.2).

3.2 Map-making

We built the survey map with a custom software, adapted from that of S-PASS for compact source detection (see Carretti 2010). For every OTF scan, data streams relative to the various feeds were detached and individually calibrated. To optimize for compact source detection, a high-pass median filtering was applied to each data stream to subtract its baseline (as suggested in Gregory et al. 1996). In particular, the filter width was set to 6.4 arcmin (corresponding to 0.6 s along the scans). This effectively removed the large-scale sky signal component, together with most of the ground emission and atmospheric fluctuations.

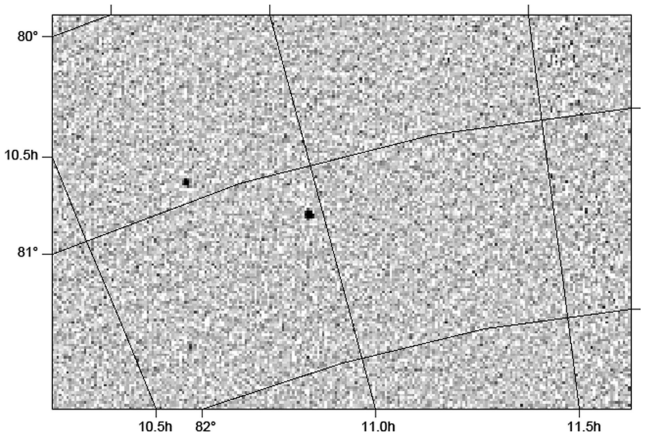

Figure 2. Small patch of the map, showing two bright sources.

Data were binned together in two different ways to be compliant with different data analysis tools. A first map was realized binning data in a HEALPIX pixelation (Górski et al. 2005). The angular resolution parameter nside was set to 4096 for pixels of size 0.85 arcmin. A second map was realized binning data on a grid of 0.8 × 0.8 arcmin^2. The gridding was performed in a zenithal equidistant projection (ARC, Calabretta & Greisen 2002) centred at the north celestial pole.

During the observations, one of the seven feeds was excluded due to hardware instabilities. This, together with the non-ideal atmospheric opacity and the occasional presence of RFI, led to a slightly higher-than-predicted noise in the final map. The scanning geometry produced an inhomogeneous sampling and a different integration time, both declination dependent, over the observed area. In particular, the high-declination inner core of the map reached a noise level of 10 mJy beam^{-1}, while the map southern edge was limited to 20 mJy beam^{-1}. The median noise level was 15.4 mJy beam^{-1}. A small patch of the map with two obvious bright sources is illustrated in Fig. 2. The scan interleave had been, due to time constraints, set to the minimum Nyquist sampling (half the beam size). This was sufficient for source detection but not suitable to obtain a photometric map for compact sources. As a consequence, follow-up observations were required for an accurate estimate of the flux densities.

3.3 Source extraction techniques

Three source extraction tools were employed to try to detect candidate sources on our map:

(i) IFCAMEX;
(ii) Signal-to-Noise-Ratio Source Extraction (SNRSE);
(iii) SExtractor.

The first software, IFCAMEX, was provided by ML-C. This code was developed in the light of the source extraction needs for maps obtained with the *Planck* satellite observations. It had demonstrated its reliability on 5-year *WMAP* maps (Massardi et al. 2009), but it had never been applied to ground-based single-dish data. Details on IFCAMEX can be found in González-Nuevo et al. (2006).

As concerns SNRSE, custom produced, here follows a brief description of its features. In order to extract the candidate sources from the surface brightness map, a sensitivity map was obtained by computing the rms noise in a 20-pixel-wide box centred around

Table 3. Average efficiency of the extraction methods on the test maps, computed for various flux density limits.

$S_{\rm lim}$ (Jy)	Injected sources	IFCAMEX detections	SNRSE detections	SExtractor detections
0.05	228	19.8	35.7	75.4
0.10	126	34.5	60.1	97.5
0.20	56	67.9	95.2	99.8
0.50	16	97.1	99.4	100.0
1.00	3	100.0	100.0	100.0
1.50	3	100.0	100.0	100.0

each pixel of the surface brightness map. By matching the sensitivity map with the surface brightness map, a list of bright pixels [with signal-to-noise ratio (S/N) > 5] was extracted. Neighbouring bright pixels were removed within a radius of one HPBW starting from the brightest and moving towards the faintest ones in order to single out candidate source positions. Finally, to improve positional and flux density accuracy, a 2D Gaussian fit was performed for each candidate source.

SExtractor (Bertin & Arnouts 1996) was employed as a third tool to extract the candidate source positions.

The three methods underwent a comparison test over semisynthetical maps. We first extracted from our map a raw list of detections with each method. We built a background map, removing from the actual map all the candidate sources and replacing them with noise pixels copied from the surroundings. Synthesized point-like sources were then injected. These sources were produced following the expected counts and flux density distribution. In total, we injected 228 sources ranging from 50 mJy to 5 Jy. We generated 10 different maps, randomly changing the spatial distribution of the sources, and performed the extraction on each of them with the three codes. Table 3 summarizes the results.

These tests indicated that SExtractor performs better than the other methods. IFCAMEX missed most of the sources with $S <$ 200 mJy; further tests are desirable to investigate the software performance when varying its set-up parameters, in order to better match the features of a map built like ours. It must be noted that, due to the distinct filters employed, each code actually listed a set of candidate sources different from the others. All the methods produced a large raw list of candidates (>4000 for SExtractor and IFCAMEX, only about 2000 for SNRSE), mainly located in the outer regions of the map, where the increasing noise adds to the effects caused by the low resolution of the map.

We then compared the detection lists achieved on the original map, containing the real sources. Discrepancies were already present at flux densities >150 mJy (10σ). Visually checking the detections on the map, we verified that none of the single methods alone was able to detect all the evident sources. This prevented us from being able to select a unique tool for the extraction.

For the sake of the follow-up phase, the three detection lists were merged and cleaned on the basis of an accurate visual inspection of the map. We easily removed artefacts due, for example, to short-time instabilities affecting the feeds, which turned into very clear marks on the map. Other features were present in areas affected by RFI. We also rejected candidates having a profile incompatible with the beam size. Due to commissioning constraints limiting the available time for the follow-up phase, the list was further restricted, by means of a stricter visual inspection, to a final selection of 151 candidate sources. This process likely introduced a bias against the faintest sources.

4 20-GHz FOLLOW-UP

Follow-up observations were carried out between 2010 December and 2011 February. They were performed in the 19–21 GHz band, to cope with RFI. Sources were almost contemporarily observed at 5 GHz. Candidates confirmed at either one of the two frequencies were then observed at 8 GHz; these multifrequency data are discussed in Paper II. Further high-frequency observations were performed, for all the sources which had been previously confirmed, in 2011 April. Candidates were this time observed using a reduced bandwidth (19.50–20.18 GHz, HPBW = 1.7 arcmin) in order to further mitigate the RFI-related effects. The source catalogue presented in this paper lists the flux densities obtained in this final session.

Table 4 summarizes the scan parameters chosen for follow-up observations. Each scan, an OTF acquisition along RA or Dec. across the source, produced an output FITS file which contained, together with several tables listing the system set-up parameters, two raw data streams (or channels) in arbitrary counts. They corresponded to the LCP and the RCP total intensities, in this case coming from the central feed of the MF receiver. All the acquired scans were visually inspected and flagged, in order to select only the suitable scans/channels for the subsequent data reduction phase. Given the point-like nature of the sources, they appeared in the scans like Gaussian profiles reproducing the antenna pattern main beam, embedded in a baseline having a linear profile (see Figs 3 and 4). Data flagging focused, as a consequence, on the selection of those scans which showed little or no alteration of the baseline and of the Gaussian profile, in order to allow a smooth integration and a good fit during the data reduction.

4.1 Data reduction

Data reduction was performed using an updated version of the OTF Scan Calibration-Reduction (OSCaR) pipeline, a customizable ensemble of IDL routines capable of handling large data sets, operating at all the frequencies available using the Medicina 32-m dish

Table 4. Follow-up scan set-up.

Frequency (GHz)	Length (arcmin)	Speed (arcmin s^{-1})	Sampling (s)
19.50–20.18	12.5	1.0	0.040

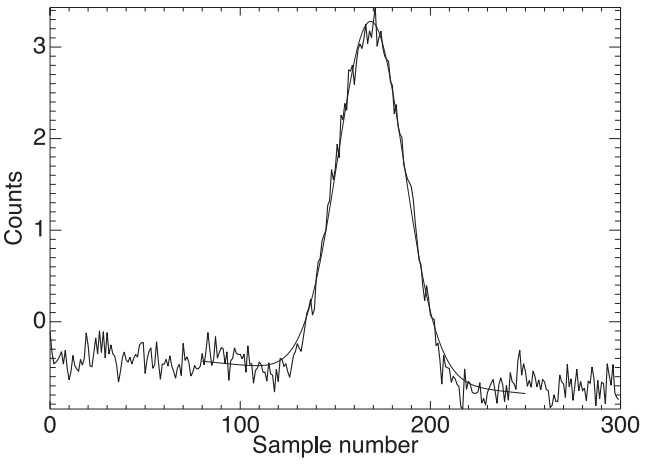

Figure 3. Portion of a single, raw OTF scan over the brightest source of the catalogue.

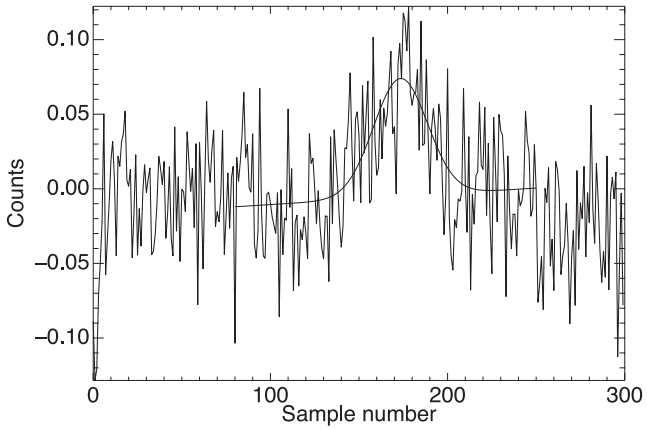

Figure 4. Portion of a single, raw OTF scan over the faintest source of the catalogue.

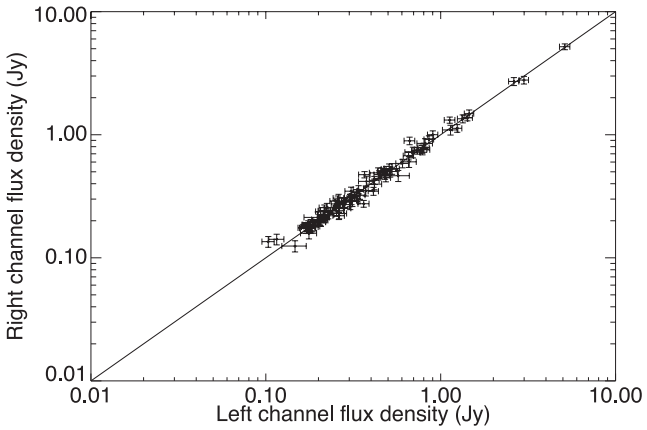

Figure 5. RCP versus LCP flux densities for the single measurements.

(see Procopio et al. 2011, for details). The main steps performed by this release of OSCaR can be summarized as follows.

(i) First, estimation of the factor to directly convert the raw signal, which is stored in arbitrary counts, to flux density units. This is obtained computing the ratio between the catalogue flux density of a calibrator (Jy) and the raw amplitude measured by means of a Gaussian fit on the scans performed on the calibrator (counts). These conversion factors are then extrapolated to the reference elevation of 90°, exploiting the antenna gain curve. They are also rescaled for the atmospheric absorption, thanks to the opacity values, which are measured from actual skydip scans obtained right after the calibration scans. This way, the conversion factors can be considered as normalized.

(ii) Reconstruction of a timeline to record the variation of the normalized counts-to-Jy factor and estimate the calibration-related error on flux density.

(iii) Association of an average counts-to-Jy factor to each set of contiguous scans on a candidate source, on the basis of the observation time. The value is then rescaled applying the antenna gain curve, i.e. taking into account the actual elevation at which the source had been observed, and the atmospheric opacity variations, which might have taken place between the calibration observation and the source observation. This conversion factor is applied once the contiguous scans have been integrated.

(iv) Fitting of a Gaussian profile over the integrated scan to measure the source flux density and estimate its uncertainty. If the source had been observed in more than one session within the analysed data set, also the globally integrated flux density is reported.

(v) Rescaling of the measured flux density, taking into account the positional offset between the position extracted from the map – and used to performed the cross-scans – and the one determined by fitting the cross-scans. This offset was generally very small, but in some cases it was as large as half the beam size – since this was the pixel size of the map.

As both the initial data flagging and the pipeline internal checks were performed on the single channels (LCP and RCP, for each scan), raw data for every cross-scan were composed of four independent estimates: LCP and RCP taken from either RA and Dec. scans. OSCaR provides an output table which lists, for each source, all the intermediate results: from the four separate estimates to the partial integrations, performed by channel and by scan direction, to the final flux density measurement. Each integration step consists of averaging the scans, weighing over their uncertainties. These uncertainties include three different contributions: (1) error due to calibration, (2) error on the amplitude measured by the Gaussian fit (usually negligible) and (3) error due to the pointing offset. The major contribution is the first (about 5 per cent on average). Thanks to the possibility of inspecting all the internal phases of the process, the final flux density measurements underwent a further selection phase. In particular, we rejected the measurements showing

(i) scans available in one direction only (RA or Dec.);
(ii) scans available in one channel only (LCP and RCP);
(iii) S/N < 5;
(iv) an unrealistic ratio between the LCP and RCP flux densities, indicating RFI contamination.

The final list contained 73 confirmed sources out of 151 candidates. Most of the sources had been observed at least twice. At the end of the selection, 21 sources preserved multiple measurements, which were averaged to obtain a final flux density for the catalogue. Fig. 5 shows the LCP and RCP flux densities for the single measurements, prior to the final averaging.

Absolute calibration was achieved considering, for the calibrators nominal flux densities, the values obtained with the polynomial models given by Baars et al. (1977). The reliability of these models was confirmed by recent observations carried out at Effelsberg (Kraus, private communication). The calibration procedure within OSCaR required at least two observations over a calibrator in one 24-h session. This goal was largely met, with the only exception of April 15, when a unique session over a calibrator positively passed the flagging phase. For that specific day, a flat calibration error equal to 5 per cent was assigned to all the measurements.

5 20-GHz CATALOGUE

The flux densities of the 73 confirmed that sources range from 115 mJy to 5 Jy. Fig. 6 shows the positions of the sources. The positional accuracy was checked using the NRAO VLA Sky Survey (NVSS) catalogue (Condon et al. 1998). A cross-match by position between the two catalogues within a search radius of 102 arcsec (one beam size) provided full matches for our catalogue (all sources have an NVSS counterpart). The displacements between the positions of our sources and their NVSS counterparts are shown in Fig. 7. The rms displacements in RA and Dec. are 15 arcsec and 13 arcsec, respectively, not far from the expected positional error of ≃1/10 of the beam size.

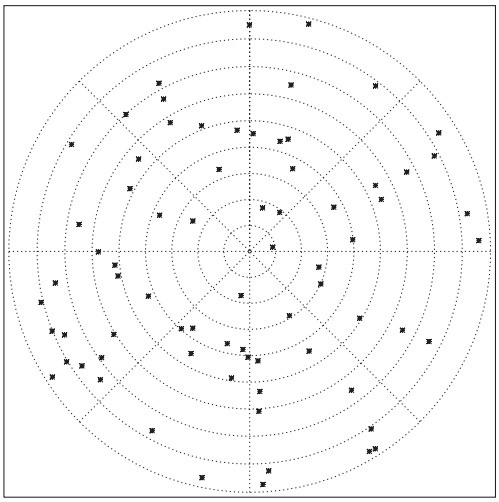

Figure 6. Positions of the confirmed sources. Map is centred on the north celestial pole, with the outer rim being Dec. = 72°. The RA = 0 h meridian is the radius pointing to the bottom side of the plot.

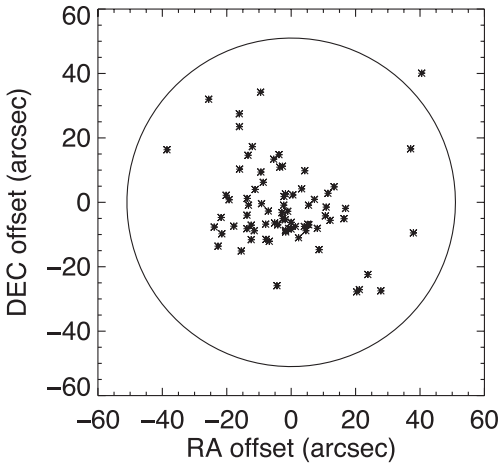

Figure 7. Position error with respect to the NVSS counterparts. The circle is one beam size in diameter (102 arcsec).

This bright catalogue was cross-matched with the 30 GHz data from the *Planck* ERCSC catalogue, obtaining 16 matches. *Planck* 30-GHz flux densities were then rescaled to 20 GHz according to individual spectral indices. These, in turn, were computed exploiting 30-GHz follow-up observations performed (in 2010 autumn) over our sources using the One Centimeter Radio Array (OCRA) system at the Toruń radio telescope – presented in Paper II together with details on the statistical and spectral properties of the sources. The resulting flux density comparison is illustrated in Fig. 8. The linear best fit is $y = 1.058x + 0.100$ (uncertainties on the two parameters are 0.084 and 0.154, respectively). Taking into account that none of the three measurements (Medicina, *Planck*, Toruń) was strictly coeval, the observed dispersion can be explained by the variability of the sources, which has a typical time-scale of weeks to months. As a check, we were able to compare the flux densities of sources KNOWS 021733+734923, KNOWS 041050+765649 and KNOWS 180044+782812 (see Table 6) with literature data. The flux densities agree to within a few per cent.

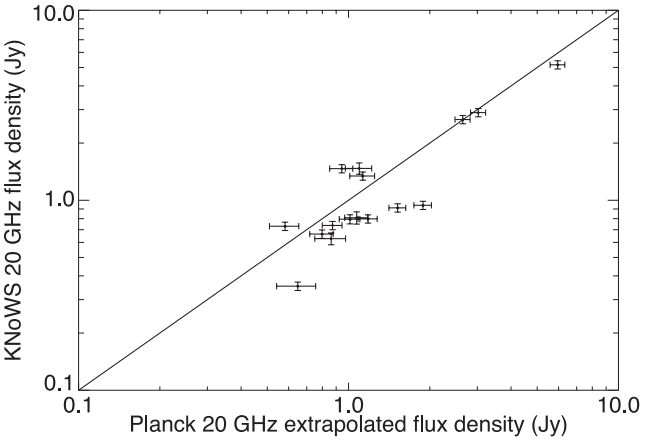

Figure 8. Comparison between KNoWS flux densities and *Planck* flux densities extrapolated to 20 GHz. Individual spectral indices were applied to each source (median value is −0.39).

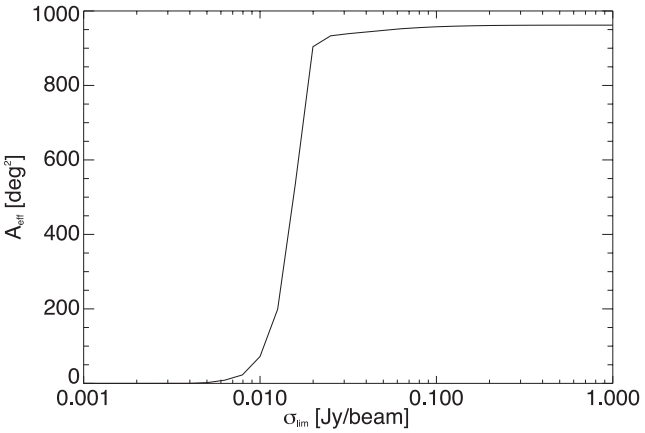

Figure 9. Effective area as a function of the map noise level.

5.1 Source counts

Source counts at 20 GHz were determined using the flux densities of the 73 sources confirmed by follow-up observations. The sensitivity map, previously used to extract candidate sources with SNRSE, was here employed to compute the visibility function of the survey – i.e. the effective area covered as a function of the survey flux density [$A_{\rm eff}(>S)$]. Fig. 9 shows how $A_{\rm eff}$ varies with the map noise level.

The counts were logarithmically binned in flux density starting from the faintest source in the catalogue. The differential counts n_i as a function of flux density have been derived as follows:

$$n_i = \frac{1}{\Delta \log(S)} \sum_{j}^{N_i} \frac{1}{A_{\rm eff}(S_j)}, \tag{2}$$

$$\log(S_i) \leq \log(S_j) < \log(S_i) + \Delta \log(S), \tag{3}$$

$$\Delta n_i = \frac{\sqrt{N_i}}{A_{{\rm eff}(S_i)}\, \Delta \log(S)}, \tag{4}$$

where n_i in equation (2) represents the number of sources N_i in the logarithmic flux density bin i defined in equation (3). The counts were weighted for the effective area $A_{\rm eff}(S_j)$ visible by each source j. Δn_i is the Poissonian error to the counts weighted for the $A_{\rm eff}$ at the flux density S_i of the bin centre. The differential counts of

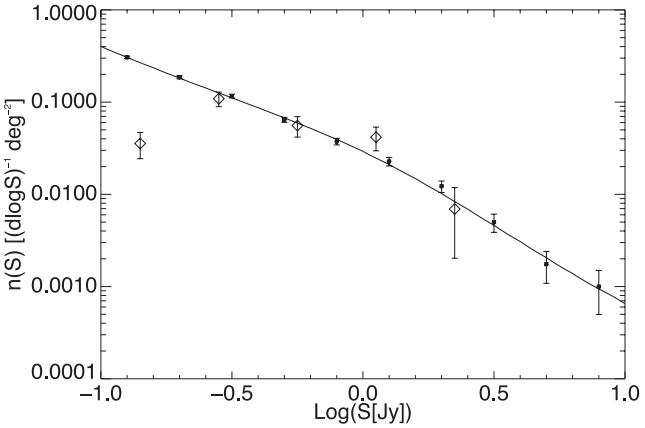

Figure 10. Differential source counts. Empty diamonds correspond to our catalogue, asterisks to the AT20G data. The solid line shows the counts predicted with the model by De Zotti et al.

Table 5. Comparison among theoretical and observed integral counts, weighted for the effective area. Poissonian errors are given in brackets for the observed counts.

$S_{\rm lim}$ (mJy)	De Zotti	KNoWS	AT20G
100	145	73 (9)	125 (11)
200	63	63 (8)	57 (8)

our catalogue in Fig. 10 are compared with the model counts by De Zotti et al. (2005) and the counts from the AT20G Full Sample catalogue. A good agreement can be seen between our counts and both the model and the AT20G counts down to the second to faintest flux density bin. Table 5 instead lists integral counts, again weighted for the effective area: our counts are compared to the ones obtained from De Zotti's model and the counts resulting within the AT20G southern polar cap (the homologous area to our survey, i.e. $-89^\circ < \delta < -73\overset{\circ}{.}2$), confirming that the completeness of our catalogue is limited to 200 mJy. This is most likely due to the bias introduced by the selection of the sources (see Section 3.3).

6 CONCLUSIONS

Our project served as a fundamental test for the hardware and software facilities which were being commissioned in Medicina. The survey/mapping initial phase and the subsequent multifrequency follow-up allowed us to deeply test the main continuum observing modes. They also helped us in improving our knowledge of the influence of RFI over high-frequency acquisitions performed with unprecedented sensitivity, as these single-dish facilities were not previously available in Medicina. Map-making, source extraction and data reduction tools, both known and custom developed, were tested and debugged, allowing us to fine-tune the whole processing phase going from data acquisition to the reduction and calibration of high-frequency maps and cross-scans (including the crucial issues related to atmospheric opacity). The survey, performed exploiting an ad hoc observing technique, produced a shallow map of the region for $\delta > 72\overset{\circ}{.}3$, with an average noise level of 15.4 mJy. A selection of the extracted source candidates was followed up, leading to the confirmation of 73 sources, down to a flux density of 115 mJy. The characteristics of the map, together with a strict selection of the source candidates imposed by the short commissioning time

Table 6. The KNoWS pilot bright sample.

Name	ID	RA (hh:mm:ss)	Dec. (°:′:″.″)	$S_{20\,\rm GHz}$ (mJy)	$\sigma_{20\,\rm GHz}$ (mJy)
KNOWS 001302+723123	1	00:13:02	72:31:22.8	325	18
KNOWS 001312+774854	2	00:13:12	77:48:54.0	208	19
KNOWS 001633+791641	3	00:16:33	79:16:40.8	247	12
KNOWS 001716+813441	4	00:17:16	81:34:40.8	745	38
KNOWS 001948+732725	5	00:19:48	73:27:25.2	1283	64
KNOWS 020313+810622	6	02:03:13	81:06:21.6	174	9
KNOWS 020336+723253	7	02:03:36	72:32:52.8	594	34
KNOWS 020649+841102	8	02:06:49	84:11:02.4	120	12
KNOWS 020954+722920	9	02:09:54	72:29:20.4	488	42
KNOWS 021733+734923	10	02:17:33	73:49:22.8	2894	145
KNOWS 022459+765544	11	02:24:59	76:55:44.4	130	11
KNOWS 035447+800918	12	03:54:47	80:09:18.0	294	21
KNOWS 041050+765649	13	04:10:50	76:56:49.2	1342	67
KNOWS 041318+745107	14	04:13:18	74:51:07.2	297	25
KNOWS 042132+835837	15	04:21:32	83:58:37.2	205	10
KNOWS 050844+843202	16	05:08:44	84:32:02.4	301	15
KNOWS 061048+724843	17	06:10:48	72:48:43.2	360	25
KNOWS 062555+820228	18	06:25:55	82:02:27.6	628	45
KNOWS 063921+732454	19	06:39:21	73:24:54.0	1467	73
KNOWS 064132+881200	20	06:41:32	88:12:00.0	204	14
KNOWS 072608+791135	21	07:26:08	79:11:34.8	498	25
KNOWS 074713+763918	22	07:47:13	76:39:18.0	498	25
KNOWS 074922+742038	23	07:49:22	74:20:38.4	416	21
KNOWS 075039+790914	24	07:50:39	79:09:14.4	240	12
KNOWS 075052+824200	25	07:50:52	82:42:00.0	475	24
KNOWS 080817+731514	26	08:08:17	73:15:14.4	320	16
KNOWS 092934+861236	27	09:29:34	86:12:36.0	187	9
KNOWS 093056+742017	28	09:30:56	74:20:16.8	240	15
KNOWS 101009+825020	29	10:10:09	82:50:20.4	353	18
KNOWS 104421+805447	30	10:44:21	80:54:46.8	1188	59
KNOWS 105359+863004	31	10:53:59	86:30:03.6	126	9
KNOWS 105812+811438	32	10:58:12	81:14:38.4	795	44
KNOWS 110149+722544	33	11:01:49	72:25:44.4	912	46
KNOWS 110410+765859	34	11:04:10	76:58:58.8	278	14
KNOWS 115311+805837	35	11:53:11	80:58:37.2	880	44
KNOWS 120019+730054	36	12:00:19	73:00:54.0	750	38
KNOWS 122340+804016	37	12:23:40	80:40:15.6	479	24
KNOWS 132143+831623	38	13:21:43	83:16:22.8	395	28
KNOWS 132351+794258	39	13:23:51	79:42:57.6	378	19
KNOWS 135324+753307	40	13:53:24	75:33:07.2	341	17
KNOWS 135756+764330	41	13:57:56	76:43:30.0	458	23
KNOWS 140638+782816	42	14:06:38	78:28:15.6	115	6
KNOWS 144830+760137	43	14:48:30	76:01:37.2	1225	61
KNOWS 152107+785837	44	15:21:07	78:58:37.2	178	9
KNOWS 155608+742107	45	15:56:08	74:21:07.2	190	11
KNOWS 160731+850159	46	16:07:31	85:01:58.8	265	13
KNOWS 160922+794023	47	16:09:22	79:40:22.8	287	22
KNOWS 163235+823228	48	16:32:35	82:32:27.6	798	40
KNOWS 172404+765328	49	17:24:04	76:53:27.6	730	37
KNOWS 180044+782812	50	18:00:44	78:28:12.0	2660	133
KNOWS 182316+793856	51	18:23:16	79:38:56.4	279	14
KNOWS 183659+750741	52	18:36:59	75:07:40.8	257	14
KNOWS 184218+794540	53	18:42:18	79:45:39.6	941	47
KNOWS 185458+735129	54	18:54:58	73:51:28.8	263	14
KNOWS 192754+735816	55	19:27:54	73:58:15.6	5165	258
KNOWS 193526+813022	56	19:35:26	81:30:21.6	193	10
KNOWS 193706+744102	57	19:37:06	74:41:02.4	420	21
KNOWS 200422+735505	58	20:04:22	73:55:04.8	308	15
KNOWS 200539+775252	59	20:05:39	77:52:51.6	809	60
KNOWS 200955+722920	60	20:09:55	72:29:20.4	737	37
KNOWS 201716+744059	61	20:17:16	74:40:58.8	464	34
KNOWS 202242+761131	62	20:22:42	76:11:31.2	1471	101

Table 6 – *continued*

Name	ID	RA (hh:mm:ss)	Dec. (°:′:″.″)	$S_{20\,GHz}$ (mJy)	$\sigma_{20\,GHz}$ (mJy)
KNOWS 204240+750802	63	20:42:40	75:08:02.4	229	12
KNOWS 211402+820437	64	21:14:02	82:04:37.2	235	12
KNOWS 213345+823904	65	21:33:45	82:39:03.6	302	15
KNOWS 220039+805844	66	22:00:39	80:58:44.4	166	12
KNOWS 220549+743632	67	22:05:49	74:36:32.4	201	10
KNOWS 230524+824232	68	23:05:24	82:42:32.4	243	17
KNOWS 231226+724055	69	23:12:26	72:40:55.2	310	23
KNOWS 231556+863130	70	23:15:56	86:31:30.0	280	19
KNOWS 232713+801236	71	23:27:13	80:12:36.0	213	16
KNOWS 234405+822638	72	23:44:05	82:26:38.4	309	15
KNOWS 235626+815255	73	23:56:26	81:52:55.2	664	34

available, produced this final catalogue of bright sources, which is complete for $S_{lim} = 200$ mJy. It must be noted that this region of the sky had never been extensively observed at 20 GHz down to this flux density limit; thus, this catalogue constitutes a useful reference for spectral studies of the listed sources. A separate paper (Paper II) illustrates the multifrequency observations and spectral analysis carried out for these sources.

ACKNOWLEDGMENTS

This work is based on observations performed with the Medicina telescope, operated by INAF – Istituto di Radioastronomia. We gratefully thank the staff at the Medicina radio telescope for the valuable support they provided. A particular acknowledgment goes to Andrea Orlati, Andrea Maccaferri and Alessandro Orfei. We warmly thank Uwe Bach and Alex Kraus of the 100-m Effelsberg telescope of the Max-Planck-Institut für Radioastronomie, who provided us with important feedback on the flux densities of calibrators prior to publication.

REFERENCES

Baars J. W. M., Genzel R., Pauliny-Toth I. I. K., Witzel A., 1977, A&A, 61, 99
Bertin E., Arnouts S., 1996, A&AS, 117, 393
Calabretta M. R., Greisen E. W., 2002, A&A, 395, 1077
Carretti E., 2010, in Kothes R., Landecker T. L., Willis A. G., eds, ASP Conf. Ser. Vol. 438, The Dynamic Interstellar Medium: A Celebration of the Canadian Galactic Plane Survey. Astron. Soc. Pac., San Francisco, p. 276
Condon J. J., Cotton W. D., Greisen E. W., Yin Q. F., Perley R. A., Taylor G. B., Broderick J. J., 1998, AJ, 115, 1693
De Zotti G., Massardi M., Negrello M., Wall J., 2010, A&AR, 18, 1
De Zotti G., Ricci R., Mesa D., Silva L., Mazzotta P., Toffolatti L., Gonzalez-Nvevo J., 2005, A&A, 431, 893
Gawroński M. P. et al., 2010, MNRAS, 406, 1853
González-Nuevo J., Argüeso F., López-Caniego M., Toffolatti L., Sanz J. L., Vielva P., Herranz D., 2006, MNRAS, 369, 1603
Górski K. M., Hivon E., Banday A. J., Wandelt B. D., Hansen F. K., Reinecke M., Bartelmann M., 2005, ApJ, 622, 759
Gregory P. C., Scott W. K., Douglas K., Condon J. J., 1996, ApJS, 103, 427
Leach S. M. et al., 2008, A&A, 491, 597
Mahony E. K., Sadler E. M., Murphy T., Ekers R. D., Edwards P. G., Massardi M., 2010, ApJ, 718, 587
Massardi M., López-Cariego M., González-Nvevo J., Herranz D., de Zotti G., Sanz J. L., 2009, MNRAS, 392, 733
Massardi M. et al., 2011, MNRAS, 412, 318
Murphy T. et al., 2010, MNRAS, 402, 2403
Orlati A., Buttu M., Migoni C., Poppi S., Righini S., 2012, Proc. SPIE Vol. 8541, The Control Software for the Sardinia Radio Telescope. SPIE, Bellingham, p. 8451-101
Planck Collaboration, 2011a, VizieR Online Data Catalog, VIII/88
Planck Collaboration, 2011b, A&A, 536, A7
Planck Collaboration, 2011c, A&A, 536, A13
Procopio P. et al., 2011, MNRAS, 417, 1123
Rohlfs K., Wilson T. L., 2006, Tools of Radio Astronomy. Springer, Berlin
Toffolatti L., Negrello M., González-Nuevo J., De Zotti G., Silva L., Granato G. L., Argüeso F., 2005, A&A, 438, 475
Wright E. L. et al., 2009a, VizieR Online Data Catalog, 218, 283
Wright E. L. et al., 2009b, ApJS, 180, 283

This paper has been typeset from a TEX/LATEX file prepared by the author.